PAPER

Check for updates

Ionic liquid-assisted growth of high-quality methylammonium lead bromide single crystals for photodetection applications†

Apurba Mahapatra, [ID] [a] Vishnu Anilkumar, [ID] [a] Joanna Kruszyńska, [ID] [a] Nada Mrkyvkova, [ID] [bc] Peter Siffalovic, [ID] [bc] Pankaj Yadav[de] and Daniel Prochowicz [ID] ★[a]

The control of nucleation temperature and growth kinetics during inverse temperature crystallization (ITC) is critical for achieving high-quality perovskite single crystals (SCs) for various optoelectronic applications. Here, we show that the addition of a 1-butyl-3-methylimidazolium bromide (BMIB) ionic liquid to the methylammonium lead bromide (MAPbBr$_3$) precursor solution not only reduces the nucleation temperature from 80 °C to 60 °C but also substantially improves the crystal quality and optoelectronic properties. Specifically, MAPbBr$_3$ SCs grown in the presence of BMIB exhibit better crystallinity with reduced lattice strain, nonradiative recombination and trap density compared to the MAPbBr$_3$ SCs grown by the conventional ITC method at 80 °C. The high quality of the BMIB-based MAPbBr$_3$ SCs enabled us to build an efficient planar-structured photodetector with high responsivity to green light (530 nm). This study shows that the ionic liquid-assisted growth of perovskite SCs has a significant influence on the crystal properties, which is beneficial for optoelectronic SC-based devices.

1. Introduction

Over the last decade, hybrid organic–inorganic lead halide perovskites (LHPs) have revolutionized the scenario of the existing semiconductor technologies due to their broad flexibility of material composition, easy bandgap tunability and outstanding optoelectronic properties.[1–4] So far, most high-efficiency LHP-based optoelectronic devices are based on polycrystalline thin films, which suffer from high defect density formed by rapid crystallization processes and severe instabilities arising from large grain boundaries.[5–8] In turn, LHPs in the form of single crystals (SCs) have been demonstrated to surmount these challenges and provide better stability, longer carrier diffusion length, lower trap density and higher charge

mobility than polycrystalline thin films.[9–13] Recently, the free-standing perovskite SCs have become a convenient platform for the next-generation optoelectronic devices including photodetectors (PDs),[14–18] electronic eyes,[19] image sensing in the medical field,[20] light emitting diodes (LEDs),[21,22] X-ray imaging,[23–25] and field effect transistors (FETs).[26]

So far, various solution-based methods such as antisolvent vapor-assisted crystallization, slow evaporation, top-seed solution method and inverse temperature crystallization (ITC) have been adopted to grow high-quality LHP SCs with different compositions and shapes.[27–31] Among them, the ITC method is particularly attractive, which is used for the rapid growth of high-quality and shape-controlled perovskite SCs within minutes by reduced solubility in different solutions at a range of elevated temperatures.[29,32,33] However, the rapid crystal growth kinetics of the ITC method at high temperatures can also lead to the formation of small crystals and affect the crystal quality.[34] The as-formed small crystals can further serve as seed nucleation sites for the growth of larger SCs. This seed-assisted growth has been widely employed in the literature as a method to yield large and high-quality LHP SCs.[35–37] Recently, Zia *et al.* reported the seed-assisted ITC method, which reduces the crystallization temperature from 80 °C to 65 °C for methylammonium lead bromide (MAPbBr$_3$) crystal growth.[38] This low-temperature seed-assisted method plays a positive role in the optical and photodetector properties of MAPbBr$_3$ SCs.

[a] *Institute of Physical Chemistry, Polish Academy of Sciences, Kasprzaka 44/52, 01-224 Warsaw, Poland. E-mail: dprochowicz@ichf.edu.pl*

[b] *Institute of Physics, Slovak Academy of Sciences, Dubravska cesta 9, 84511 Bratislava, Slovakia*

[c] *Center for Advanced Materials and Applications, Slovak Academy of Sciences, Dubravska cesta 9, 84511 Bratislava, Slovakia*

[d] *Department of Solar Energy, School of Energy Technology, Pandit Deendayal Energy University, Gandhinagar-382 007, Gujarat, India*

[e] *Department of Physics, School of Energy Technology, Pandit Deendayal Energy University, Gandhinagar-382 007, Gujarat, India*

† Electronic supplementary information (ESI) available. See DOI: **https://doi.org/10.1039/d3tc04511k**

This journal is © The Royal Society of Chemistry 2024

J. Mater. Chem. C, 2024, **12**, 2953–2960 | 2953

However, this requires a two-step crystallization process, which increases the complexity and cost of the overall process. To address this issue, changing the crystallization environment was proposed as an efficient method to produce large LHP SCs with high quality at low temperatures. For example, the addition of formic acid[39–41] or 3-(decyldimethylammonio)-propane-sulfonate inner salt (DPSI)[42] to a perovskite precursor solution facilitates the rapid growth of high-quality SCs with reduced defect density and enables crystallization at lower temperatures without the help of the seed crystals. Recent works revealed that the addition of ionic liquids (ILs) to the perovskite precursor solution improves the crystallization propensity for the acquisition of high-quality polycrystalline perovskite films with a low number of defects.[43,44] Due to the hybrid structures of anions and cations, ILs can form strong hydrogen and coordination bonds in solution with the perovskite components, modifying the crystallization kinetics.[45,46] However, to the best of our knowledge, the use of ILs for the controlled growth of LHP SCs has not been reported.

Here, we show that the addition of a 1-butyl-3-methylimidazolium bromide (BMIB) IL to the MAPbBr$_3$ precursor solution is promising for the growth of high-quality MAPbBr$_3$ SCs and for reducing the nucleation temperature from 80 °C to 60 °C. First, the effect of various BMIB concentrations on the nucleation time, crystallization rate and growth temperature of MAPbBr$_3$ SCs was examined. It was found that the presence of an optimized amount of BMIB IL facilitated the self-assembly and crystallization process *via* the formation of PbBr$_2$–ionic liquid complexes, which reduced the crystallization kinetics for the growth of large SCs. X-ray diffraction (XRD) analysis revealed a reduced lattice strain in MAPbBr$_3$ SCs grown in the presence of BMIB compared to the MAPbBr$_3$ SCs obtained using the conventional ITC method at 80 °C. In addition, the BMIB-based MAPbBr$_3$ SC exhibits better optical and electrical properties, which further confirms their high quality and potential for utilization in photodetection. A planar-structured PD based on a BMIB-based MAPbBr$_3$ SC exhibits responsivity and EQE as high as 4.81 A W^{-1} and 1124% under green light (530 nm) at 2 V bias, respectively. These values are much better than those of the device based on the MAPbBr$_3$ SC formed by the conventional ITC method at 80 °C.

2. Results and discussion

The molecular structure of the ionic liquid (BMIB) used in this study is shown in Fig. S1 (ESI†). MAPbBr$_3$ SCs were grown using the ITC method, as previously reported.[47,48] For this conventional nucleation growth, a 1.2 M MAPbBr$_3$ precursor solution in DMF was heated to a temperature of 80 °C at a ramp of 20 °C h^{-1}. It was observed that almost 30 min were required to start the nucleation process at 80 °C, and SCs with the desired dimensions of ~4 × 4 × 2 mm^3 were observed after continuing crystallization for 4 h (Fig. 1a and Fig. S2, ESI†). We also tested the crystallization process of a 1.2 M MAPbBr$_3$ precursor solution at a lower temperature (60 °C); however, at this
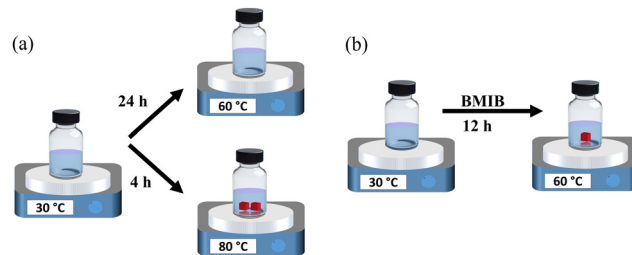

Fig. 1 Schematic of the crystallization procedure of the MAPbBr$_3$ SC (a) without and (b) with BMIB.

temperature, SCs were not observed even after 24 h. This is consistent with the work of Liu *et al.*, where ~18 days were required to reach sufficient supersaturation for the nucleation and growth of MAPbBr$_3$ SCs at a lower temperature of 60 °C.[49] For crystal growth with the IL additive, BMIB was added to the perovskite precursor solution at various concentrations (1, 3, 5 and 10 mol%) (Fig. 1b). The temperature for crystallization was set as 60 °C using a ramp of 20 °C h^{-1}. The nucleation time (after reaching 60 °C) varied with increasing the concentration of BMIB, as shown in Table S1 (ESI†). It was observed that SCs with desired dimensions were obtained from the precursor solution with 5 mol% BMIB after growing for 12 h (Fig. S3, ESI†). With lower concentrations of BMIB (1 mol% and 3 mol%), only small crystallites were formed after 12 h due to the very slow crystallization rate (Fig. S4, ESI†). However, increasing the BMIB concentration to 10 mol% failed to initiate the nucleation at 60 °C.

It is known that the growth of SCs is generally controlled by the diffusion rate of the solute in the solution and the solute deposition rate on the crystal surface.[38] The diffusion rate in solution exponentially increases with increasing the temperature according to eqn (1):

$$D = D_0 \exp\left(-\frac{\Delta H}{RT}\right) \qquad (1)$$

where D is the diffusion rate, ΔH is the diffusion activation rate, D_0 is the diffusion constant, T is the solution temperature and R is the gas constant. Therefore, a high diffusion rate at high temperatures (80 °C) can lead to the formation of SCs with defects and imperfections.[29,50] To control the crystal growth quality at low temperatures, it is important to find a balance between the diffusion rate and solute deposition rate. The addition of 5% BMIB to the MAPbBr$_3$ precursor solution helped to overcome the nucleation energy for the formation of nuclei at a low temperature of 60 °C and assisted in growing crystals below the supersaturation limit. To further investigate the effect of 5 mol% of BMIB on the crystallization rate, we attempted the crystallization of MAPbBr$_3$ SCs with and without the BMIB additive at 80 °C (Fig. S5, ESI†). The time required to start the nucleation process for the precursor solution with BMIB was around ~60 min, which is much longer than the nucleation time (~30 min) for the precursor solution without BMIB. The prolonged nucleation process in the precursor solution with BMIB could be attributed to the interactions

2954 | *J. Mater. Chem. C*, 2024, **12**, 2953–2960

This journal is © The Royal Society of Chemistry 2024

between the BMIB and perovskite component, which restrict the diffusion of ions and affect the growth rate of MAPbBr$_3$ SCs (*vide infra*). To compare the crystallization rate, we continued the crystallization process for the next 6 h after the nucleation process. As seen in Table S2 (ESI†), the addition of BMIB to the perovskite solution decreases the growth rate and allows control over the formation of SCs in the ITC process.

The change in the crystal growth kinetics of the MAPbBr$_3$ SC by the addition of BMIB could affect its crystal structure and quality. To confirm this, we first checked whether BMIB existed in the bulk and/or at the surface of the MAPbBr$_3$ SC using liquid-state ^{1}H NMR spectroscopy. As shown in Fig. S6 (ESI†), the lack of characteristic signals of BMIB in the respective NMR spectra indicates that this additive does not exist in the crystal structure. However, BMIB molecules may interact with the perovskite component (PbBr$_2$) in the precursor solution *via* hydrogen bonding interactions[51] and influence the crystallization process by decreasing the solute diffusion rate.[38,50] Fig. S7 (ESI†) shows the ^{1}H NMR spectrum of the simple reaction between BMIB and PbBr$_2$ in a 1:1 molar ratio. As seen, the peak belonging to BMIB at 9.18 ppm shifts toward the

high field region to 9.11 ppm after the addition of PbBr$_2$, which suggests the formation of salt [BMI]PbBr$_3$, as revealed by Zhang *et al.*[51] XRD analysis was further conducted to study the effect of BMIB on the crystal structure and crystallinity of the MAPbBr$_3$ SC. The XRD patterns of the maximal facet for both MAPbBr$_3$ SCs showed characteristic peaks along (100), (200), and (300) planes, confirming their high purity (Fig. 2a). However, the much stronger intensities of these peaks for the BMIB-based MAPbBr$_3$ SC suggests superior crystallinity. Furthermore, the full width at half-maximum (FWHM) analysis of the three major peaks can provide the lattice strain using the tangent formula (see Supplementary Note 1, ESI†).[52] The FWHM and lattice strain values of both SCs are summarized in Table S3 (ESI†). As seen, low FWHM was found for the BMIB-based MAPbBr$_3$ SC, which indicates a reduced lattice strain within this SC. The reduced lattice strain is beneficial for decreasing ion migration within the perovskite crystal and nonradiative recombination processes.[38,53]

The trap states located within the band gap of perovskite materials play a critical role of undesirable obstacles in all photophysical applications.[31] To shed more light on the energy

Fig. 2 (a) XRD patterns and (b) steady-state photoluminescence spectra of the reference and BMIB-based MAPbBr$_3$ SCs. Pulsed voltage SCLC $I–V$ measurement curves for all three regimes of the (c) reference and (d) BMIB-based MAPbBr$_3$ SCs. (e) Trap density (η), (f) mobility (μ) and (g) time-resolved photoluminescence (TRPL) of the reference and BMIB-based MAPbBr$_3$ SCs. (h) Carrier lifetime and (i) diffusion length (L_D) statistics for each type of studied SCs.

This journal is © The Royal Society of Chemistry 2024

J. Mater. Chem. C, 2024, **12**, 2953–2960 | **2955**

states and defects, photoluminescence (PL) measurements were performed on both types of SCs. As shown in Fig. 2b, the PL spectra exhibit a sharp peak at 542 nm (2.29 eV) with no shift in the peak position, which is consistent with the literature.[38,50] Notably, the BMIB-based $MAPbBr_3$ SC exhibited an enhanced PL intensity compared to the reference $MAPbBr_3$ SC, which indicates suppression of the nonradiative recombination in the modified SC. These results further support our findings from the XRD analysis.

Next, we investigated the charge transport and electronic properties of these SCs using the space charge-limited current (SCLC) method.[31,54] The values of conductivity (σ), trap density (η_{trap}) and mobility (μ) were calculated by recording the dark current of the Pt/SC/Pt hole-only devices with a vertical geometry. The pulsed voltage sweep SCLC method was used to minimize the ion migration effect during the measurement.[55] Fig. 2c and d displays the dark I–V characteristics of the reference and BMIB-based $MAPbBr_3$ SCs. Both dark I–V curves exhibit three distinct regions marked as ohmic, trap-filling and child regions. The conductivity (σ) of both types of SCs was calculated from the ohmic region, and the BMIB-based $MAPbBr_3$ SC shows a higher value of σ than the reference $MAPbBr_3$ SC (Fig. S8, ESI†). For the trap-filling region and considering a linear dependence between η_{trap} and the trap-filled limit voltage (V_{TFL}), the hole densities (η_h) are calculated using eqn (2):[31]

$$\eta_{trap} = \frac{2\varepsilon_r \varepsilon_0 V_{TFL}}{eL^2} \qquad (2)$$

where ε, L, ε_0 and e are the dielectric constant, thickness of the crystals, vacuum permittivity and elementary charge, respectively. To minimize the error in the measurement, we tested six separate reference and BMIB-based $MAPbBr_3$ SCs. The average η_{trap} was found to be $2.07 \pm 0.11 \times 10^9$ cm^{-3} for the reference $MAPbBr_3$ SC, while the values of η_{trap} decreased by $\sim$40% and were equal to $1.2 \pm 0.08 \times 10^9$ cm^{-3} for the BMIB-based $MAPbBr_3$ SC (Fig. 2e). The carrier mobility (μ) for holes in the SCs studied can also be calculated from the trap-filled SCLC regions of hole-only devices using the Mott–Gurney law (3):

$$\mu = \frac{8 J_d L^3}{9 \varepsilon \varepsilon_0 V^2} \qquad (3)$$

where J_d and V are the dark current density and the applied bias, respectively. As expected, the BMIB-based $MAPbBr_3$ SC exhibits a high average μ of 63.9 ± 5.4 cm^2 V^{-1} s^{-1}, which is more than two times higher than μ calculated for the reference $MAPbBr_3$ SC (23.8 ± 3.4 cm^2 V^{-1} s^{-1}) (Fig. 2f). The ultralow trap density and high carrier mobility indicate the excellent quality of the BMIB-based $MAPbBr_3$ SC.

To study the recombination dynamics of the photoexcited species, both SCs were investigated by time-resolved PL (TRPL) spectroscopy. We fitted the decay curves using the biexponential decay with a fast component (τ_1) and a slow component (τ_2). The fast (τ_1) and slow (τ_2) decay components are associated with the nonradiative recombination arising from the surface defects and bulk radiative recombination, respectively.[56] As shown in Fig. 2g, the BMIB-based $MAPbBr_3$ SC ($\tau_1 = 3$ ns and $\tau_2 = 43$ ns) exhibits a

longer carrier lifetime than the reference $MAPbBr_3$ SC ($\tau_1 = 2$ ns and $\tau_2 = 21$ ns). As can be seen, the fast and slow components are longer for the BMIB-based $MAPbBr_3$ SC, which suggests reduced surface and bulk nonradiative recombination in this type of crystal. It can be observed that the difference between the carrier lifetimes is very small, and the values change with changes in the measurement position, excitation wavelength, crystalline plane, and measurement time.[57–59] Therefore, we investigated three individual crystals for each type of sample and collected time-resolved PL (TRPL) decay for a longer decay time scale to calculate the diffusion length (L_D) (Fig. S9, ESI†). The fitted decay curves show three decay components (two fast components and one slow component). The statistical distributions of the average fast and slow components for each crystal are shown in Fig. 2h. As can be seen, the average fast component is almost the same for both types of SCs. The slow component is longer for the BMIB-based $MAPbBr_3$ SC, which suggests a reduced bulk nonradiative recombination in this type of crystal. Based on the calculated μ and τ, the diffusion length (L_D) for each SC can be estimated using eqn (4):[29]

$$L_D = \sqrt{(k_B T / e) \times \mu\tau} \qquad (4)$$

where k_B and T are the Boltzmann constant and the temperature, respectively. The average L_D values based on the fast and slow components of the carrier lifetime are 1.72 ± 0.18 μm and 4.46 ± 0.47 μm for the BMIB-based $MAPbBr_3$ SC, while those for the reference $MAPbBr_3$ SC are 2.88 ± 0.15 μm and 9.74 ± 0.52 μm respectively (Fig. 2i). The values of L_D in the BMIB-based $MAPbBr_3$ SC are $\sim$2 times higher than those of reference $MAPbBr_3$ SC, which supports its better quality and optoelectronic properties.

For high-performance optoelectronic devices, especially in SC-based PDs, the quality of the active material and its optoelectronic properties play a significant role. Having in hand the high-quality $MAPbBr_3$ SC, we fabricated planar-type PDs by depositing Pt electrodes on the surfaces of reference and BMIB-based $MAPbBr_3$ SCs according to our previous study (for the device fabrication, see the Experimental section).[47] First, we collected the I–V characteristics under dark conditions, as shown in Fig. 3a. As can be seen, BMIB-based PD exhibits a higher dark current (I_d) than that of the reference PD. The observed higher I_d may primarily suggest the presence of a high defect density in the BMIB-based $MAPbBr_3$ SC.[38,50] However, our results reveal that the values of η_{trap} are lower in the BMIB-based $MAPbBr_3$ SC than in the reference $MAPbBr_3$ SC (Fig. 2e). Thus, we attributed the higher I_d to the high conductivity and hole mobility of the BMIB-based $MAPbBr_3$ SC. The quality of the PDs was further verified by analyzing the photocurrent under light and an applied bias. The photocurrent (I_{ph}) increases with increasing bias for each type of PD, and the BMIB-based PD exhibits a higher I_{ph} than the reference PD.

As the halide perovskites are known to exhibit hysteretic behaviour due to ion migration,[12,60] we studied the effect of BMIB on hysteresis in PD. Fig. S10 (ESI†) shows the comparison of the I–V characteristics measured in forward and reverse scan
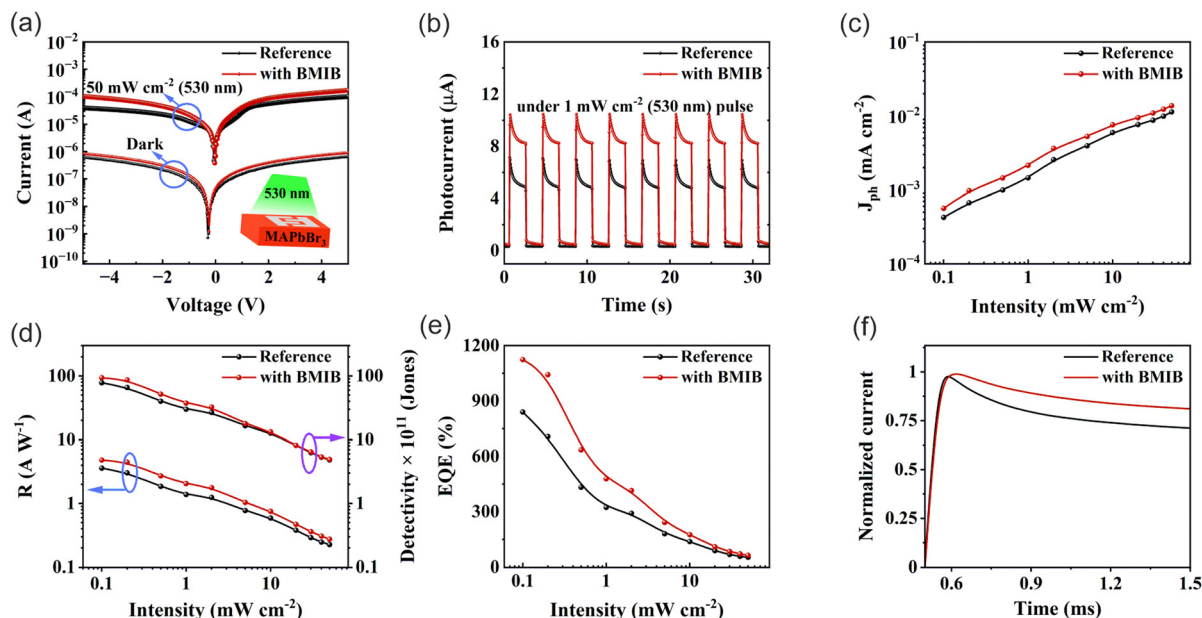
Fig. 3 (a) Dark and light $I-V$ characteristics. (b) Current–time ($I-t$) characteristics of the reference and BMIB-based PDs. (c) Photocurrent density (J_{ph}), (d) R (left axis), D^* (right axis), (e) EQE and (f) normalized transient photocurrent of the reference and BMIB-based PDs under green light at 2 V.

directions at a 100 mV s^{-1} scan rate under a 50 mW cm^{-2} illumination. The lower difference in the current under forward and reverse bias ($\Delta I = I_{backward} - I_{forward}$) for the BMIB-based PD suggests reduced ion migration, which is beneficial for a stable performance. To shed more light on PD performance, we measured the transient photoresponses of both the PDs under a green LED ($\lambda = 530$ nm) light pulse with irradiance power densities ranging from 0.1 to 50 mW cm^{-2} at a fixed bias voltage of 2 V (Fig. S11, ESI†). The current–time ($I-t$) characteristics of each type of PD at a 1 mW cm^{-2} irradiance power are shown in Fig. 3b. The observed overshooting sharp transient peaks followed by photocurrent decay for a longer time scale in both $I-t$ curves could be due to the dominant effect of the charge recombination and ion accumulation near the electrode with negligible effect of carrier trapping under the green light.[61] The observed higher photocurrent on the BMIB-based PD indicates better photogenerated charge separation due to lower nonradiative recombination. The logarithmic photocurrent density (J_{ph}) as a function of incident light intensity for each type of PD is shown in Fig. 3c. As can be seen, the values of J_{ph} increase with increasing intensity of the incident light due to the increase in the charge generation rate. Notably, the BMIB-based PD generated almost 30% higher J_{ph} than the reference MAPbBr$_3$ SC-based PD, which suggests its improved performance. The responsivity (R), specific detectivity (D^*), and external quantum efficiency (EQE) of the studied device were calculated using eqn (S3), (S4) and (S5), respectively (see Supplementary Note 2, ESI†). From Fig. 3d and e, we can observe that the BMIB-based PD exhibits higher R and EQE than the reference MAPbBr$_3$ SC-based PD. The maximum R and EQE increases to 4.81 A W^{-1} and 1124% for the BMIB-based PD compared to the reference MAPbBr$_3$ SC-based PD (3.5 A W^{-1} and 839%) under a green light of 0.1 mW cm^{-2}. However, there

was no significance difference in the values of D^*, and the higher I_d of the BMIB-based PD did not affect the overall performance of the PDs. The improved photodetection properties of the BMIB-based PD can also be attributed to longer L_D, which plays a vital role in the extraction of photogenerated charge carriers and directly controls the responsivity of PDs.[47]

The decay behaviour of transient photoresponse of the MAPbBr$_3$ SC-based PDs could give important information about charge recombination and ion accumulation under green light and bias.[61] The normalized spectra of transient photocurrent decay of each type of PD at a 1 mW cm^{-2} irradiance power are shown in Fig. 3f. The observed slower photocurrent decay under green light on the BMIB-based PD indicates a lower level of charge recombination and ion accumulation than that of the reference MAPbBr$_3$ SC-based PD. The response time depends on the capacity of PDs to follow the rapidly changing optical signals. The rise-time (τ_{on}, from 10% to 90% of the saturated values) and fall-time (τ_{off}, from 90% to 10% of the saturated values) for each type of PD were extracted from the normalized photoresponse characteristics, as shown in Fig. S12. The BMIB-based PD exhibits faster response time ($\tau_{on} = 12.1$ ms, $\tau_{off} = 14.8$ ms) compared to the reference MAPbBr$_3$ SC-based PD with $\tau_{on} = 14.3$ ms and $\tau_{off} = 16.1$ ms due to higher conductivity and mobility, which allows faster transport of the photogenerated charge carrier. The operational stability of PDs under continuous operation is an essential requirement from the commercialization perspective. The functional stability of the PDs is shown in Fig. S13 (ESI†). The output of both PDs is stable ($\sim 92\%$ performance remaining after 24 h of continuous operation under a 1 mW cm^{-2} optical signal), which is comparable with the previous studies.[47,62] These results confirm that the BMIB-based MAPbBr$_3$ SC can be an efficient

This journal is © The Royal Society of Chemistry 2024

J. Mater. Chem. C, 2024, **12**, 2953–2960 | **2957**

semiconducting material for the fabrication of devices with excellent PD performance.

3. Conclusions

In summary, we have demonstrated a modified ITC approach to grow high-quality MAPbBr$_3$ SCs through the addition of BMIB to the perovskite precursor solution, which allowed crystallization to occur at 60 °C. The addition of BMIB was found to facilitate the self-assembly and crystallization processes *via* the formation of PbBr$_2$–ionic liquid complexes, which reduces the crystallization kinetics for the growth of large MAPbBr$_3$ SCs. The structural, optical and electrical properties of the as-formed BMIB-based MAPbBr$_3$ SC were studied and compared to those of the MAPbBr$_3$ SC obtained by using conventional ITC method at 80 °C. The results revealed that BMIB-based MAPbBr$_3$ SCs exhibited enhanced crystallinity with reduced lattice strain, nonradiative recombination and trap density, which make them attractive for photodetection applications. The planar PD with a structure of Pt/MAPbBr$_3$ SC/Pt exhibited an R of 4.81 A W^{-1}, EQE of 1124% and response time of 12.1 ms under 0.1 mW cm^{-2} green light (530 nm) and a 2 V bias, which are higher than those of the device based on the MAPbBr$_3$ SC formed using the conventional ITC method at 80 °C and comparable to previously reported studies on MAPbBr$_3$ SC-based PDs (Table S4, ESI†). The superior performance can be attributed to the observed high mobility, conductivity and diffusion length of the BMIB-based MAPbBr$_3$ SC. We believe that the use of a low-temperature ITC method for the growth of high-quality MAPbBr$_3$ SCs will lead to the development of a new generation of SC-based optoelectronic devices.

4. Experimental section

4.1. Materials

Lead(II) bromide (PbBr$_2$, ≥98%) and dimethyl formamide (DMF, anhydrous 99.8%) were obtained from Sigma-Aldrich, methylammonium bromide (MABr, >99.99%) was obtained from Great Cell Solar Materials, and 1-butyl-3-methylimidazolium bromide IL (BMIB, >98%) was obtained from Sigma-Aldrich. All chemicals were used as received without any further purification.

4.2. Synthesis and characterization of SCs

Synthesis of MAPbBr$_3$ SCs without and with BMIB ILs. Equimolar amounts of MABr (1344 mg) and PbBr$_2$ (4404 mg) were dissolved in 10 mL of DMF to make a 1.2 M solution. After complete dissolution, the mixture was filtered using a PTFE 0.2 µm filter, divided into 3 different vials, and slowly heated to 80 °C. After 8 h, SCs with sizes over 4 × 4 × 2 mm were crystallized, dried and used for further measurements. To synthesize MAPbBr$_3$ with the BMIB IL, 1 (26 mg), 3 (79 mg), 5 (131 mg) and 10 (263 mg) mol% of BMIB IL were added to 10 mL 1.2 M precursor solution of MAPbBr$_3$. After complete dissolution, the solution was filtered using a PTFE 0.2 µm filter, divided into three vials, and slowly heated to 60 °C. After 12 h, SCs

with sizes over 4 × 4 × 2 mm were formed, dried and used for further measurements.

X-ray diffraction on SCs was performed using an Empyrean diffractometer (PANalytical) using a copper lamp (40 kV, 40 mA) with 2θ of over 10° to 50°, keeping the SC sample stationary. Steady-state photoluminescence spectra were collected using a Shimadzu RF-6000 spectrometer. Transiently resolved photoluminescence (TRPL) spectra were recorded using an Edinburgh Instrument (FLS1000). For SCLC measurements, vertical devices were made by sputtering Pt electrodes on the crystal's top face and opposite bottom face from 0 to 10 V with a step voltage of 25 mV. A short time voltage pulse (20 ms) was followed by a long rest time at 0 V (2 min).

4.3. Fabrication and characterization of the MAPbBr$_3$ SC-based PDs

A 60 nm thick platinum (Pt) electrode was deposited over the (100) facets of the SCs using a spluttered magnetron (Leica EM MED020) with the help of a self-designed mask with a 150 µm channel. All dark J–V and PD response measurements were performed using a LASC probe station connected to a Bio-Logic SP-150e potentiostat at a scan rate of 100 mV s^{-1}. Using Thorlabs GmbH, PM 100D, the illumination power of a green LED (Luxeon Star LEDs) was optimized.

Author contributions

A. M. – investigation, methodology, writing – original draft; V. A. – investigation, data curation; J. K. – formal analysis, visualization; N. M. – data curation, formal analysis; P. S. – data curation, formal analysis; P. Y. – formal analysis; D. P. – conceptualization, supervision, writing – review and editing.

Conflicts of interest

There are no conflicts to declare.

Acknowledgements

References

1 J. Miao and F. Zhang, *J. Mater. Chem. C*, 2019, **7**, 1741–1791.
2 M. Ahmadi, T. Wu and B. Hu, *Adv. Mater.*, 2017, **29**, 1605242.
3 Z. Yi, N. H. Ladi, X. Shai, H. Li, Y. Shen and M. Wang, *Nanoscale Adv.*, 2019, **1**, 1276–1289.
4 L. Chouhan, S. Ghimire, C. Subrahmanyam, T. Miyasaka and V. Biju, *Chem. Soc. Rev.*, 2020, **49**, 2869–2885.

2958 | *J. Mater. Chem. C*, 2024, **12**, 2953–2960

This journal is © The Royal Society of Chemistry 2024

5 W. A. Dunlap-Shohl, Y. Zhou, N. P. Padture and D. B. Mitzi, *Chem. Rev.*, 2019, **119**, 3193–3295.

6 J. Sun, J. Wu, X. Tong, F. Lin, Y. Wang and Z. M. Wang, *Adv. Sci.*, 2018, **5**, 1700780.

7 T. S. Sherkar, C. Momblona, L. Gil-Escrig, J. Ávila, M. Sessolo, H. J. Bolink and L. J. A. Koster, *ACS Energy Lett.*, 2017, **2**, 1214–1222.

8 W. Fu, A. G. Ricciardulli, Q. A. Akkerman, R. A. John, M. M. Tavakoli, S. Essig, M. V. Kovalenko and M. Saliba, *Mater. Today*, 2022, **58**, 275–296.

9 S. D. Stranks, G. E. Eperon, G. Grancini, C. Menelaou, M. J. P. Alcocer, T. Leijtens, L. M. Herz, A. Petrozza and H. J. Snaith, *Science*, 2013, **342**, 341–344.

10 Q. Dong, Y. Fang, Y. Shao, P. Mulligan, J. Qiu, L. Cao and J. Huang, *Science*, 2015, **347**, 967–970.

11 X.-D. Wang, W.-G. Li, J.-F. Liao and D.-B. Kuang, *Solar RRL*, 2019, **3**, 1800294.

12 A. Mahapatra, R. Runjhun, J. Nawrocki, J. Lewiński, A. Kalam, P. Kumar, S. Trivedi, M. M. Tavakoli, D. Prochowicz and P. Yadav, *Phys. Chem. Chem. Phys.*, 2020, **22**, 11467–11473.

13 S. Trivedi, D. Prochowicz, N. Parikh, A. Mahapatra, M. K. Pandey, A. Kalam, M. M. Tavakoli and P. Yadav, *ACS Omega*, 2021, **6**, 1030–1042.

14 Y. Zhang, Y. Liu and S. (Frank) Liu, *Adv. Funct. Mater.*, 2023, **33**, 2210335.

15 J. Li, Y. Gu, Z. Han, J. Liu, Y. Zou and X. Xu, *J. Phys. Chem. Lett.*, 2022, **13**, 274–290.

16 J. Zhou and J. Huang, *Adv. Sci.*, 2018, **5**, 1700256.

17 L. Lu, W. Weng, Y. Ma, Y. Liu, S. Han, X. Liu, H. Xu, W. Lin, Z. Sun and J. Luo, *Angew. Chem., Int. Ed.*, 2022, **134**, e202205030.

18 Y. Ma, W. Guo, Q. Fan, H. Xu, L. Tang, Y. Liu, W. Li, X. Liu, J. Luo and Z. Sun, *Adv. Funct. Mater.*, 2023, **33**, 2210235.

19 Q. Wang, G. Zhang, H. Zhang, Y. Duan, Z. Yin and Y. Huang, *Adv. Funct. Mater.*, 2021, **31**, 2100857.

20 L. Li, S. Ye, J. Qu, F. Zhou, J. Song and G. Shen, *Small*, 2021, **17**, 2005606.

21 X. Zhao, S. Wang, X. Shan, G. Meng and X. Fang, *Cryst. Growth Des.*, 2021, **21**, 5983–5997.

22 Y. Cho, H. R. Jung and W. Jo, *Nanoscale*, 2022, **14**, 9248–9277.

23 Z. Pan, L. Wu, J. Jiang, L. Shen and K. Yao, *J. Phys. Chem. Lett.*, 2022, **13**, 2851–2861.

24 K. Sakhatskyi, B. Turedi, G. J. Matt, E. Wu, A. Sakhatska, V. Bartosh, M. N. Lintangpradipto, R. Naphade, I. Shorubalko, O. F. Mohammed, S. Yakunin, O. M. Bakr and M. V. Kovalenko, *Nat. Photonics*, 2023, **17**, 510–517.

25 Z. Zhang, H. Li, H. Di, D. Liu, W. Jiang, J. Ren, Z. Fan, F. Liao, L. Lei, G. Li, Y. Xiong and Y. Zhao, *ACS Appl. Electron. Mater.*, 2023, **5**, 388–396.

26 W. Yu, F. Li, L. Yu, M. R. Niazi, Y. Zou, D. Corzo, A. Basu, C. Ma, S. Dey, M. L. Tietze, U. Buttner, X. Wang, Z. Wang, M. N. Hedhili, C. Guo, T. Wu and A. Amassian, *Nat. Commun.*, 2018, **9**, 5354.

27 D. Shi, V. Adinolfi, R. Comin, M. Yuan, E. Alarousu, A. Buin, Y. Chen, S. Hoogland, A. Rothenberger, K. Katsiev, Y. Losovyj, X. Zhang, P. A. Dowben, O. F. Mohammed, E. H. Sargent and O. M. Bakr, *Science*, 2015, **347**, 519–522.

28 A. A. Zhumekenov, V. M. Burlakov, M. I. Saidaminov, A. Alofi, M. A. Haque, B. Turedi, B. Davaasuren, I. Dursun, N. Cho, A. M. El-Zohry, M. De Bastiani, A. Giugni, B. Torre, E. Di Fabrizio, O. F. Mohammed, A. Rothenberger, T. Wu, A. Goriely and O. M. Bakr, *ACS Energy Lett.*, 2017, **2**, 1782–1788.

29 Y. Liu, Y. Zhang, Z. Yang, J. Feng, Z. Xu, Q. Li, M. Hu, H. Ye, X. Zhang, M. Liu, K. Zhao and S. (Frank) Liu, *Mater. Today*, 2019, **22**, 67–75.

30 Y. Liu, X. Zheng, Y. Fang, Y. Zhou, Z. Ni, X. Xiao, S. Chen and J. Huang, *Nat. Commun.*, 2021, **12**, 1686.

31 A. Mahapatra, D. Prochowicz, J. Kruszyńska, S. Satapathi, S. Akin, H. Kumari, P. Kumar, Z. Fazel, M. Mahdi Tavakoli and P. Yadav, *J. Mater. Chem. C*, 2021, **9**, 15189–15200.

32 W. Wang, H. Meng, H. Qi, H. Xu, W. Du, Y. Yang, Y. Yi, S. Jing, S. Xu, F. Hong, J. Qin, J. Huang, Z. Xu, Y. Zhu, R. Xu, J. Lai, F. Xu, L. Wang and J. Zhu, *Adv. Mater.*, 2020, **32**, 2001540.

33 M. I. Saidaminov, A. L. Abdelhady, B. Murali, E. Alarousu, V. M. Burlakov, W. Peng, I. Dursun, L. Wang, Y. He, G. Maculan, A. Goriely, T. Wu, O. F. Mohammed and O. M. Bakr, *Nat. Commun.*, 2015, **6**, 7586.

34 Z. Lian, Q. Yan, T. Gao, J. Ding, Q. Lv, C. Ning, Q. Li and J. Sun, *J. Am. Chem. Soc.*, 2016, **138**, 9409–9412.

35 Y. Liu, J. Sun, Z. Yang, D. Yang, X. Ren, H. Xu, Z. Yang and S. (Frank) Liu, *Adv. Opt. Mater.*, 2016, **4**, 1829–1837.

36 W.-G. Li, H.-S. Rao, B.-X. Chen, X.-D. Wang and D.-B. Kuang, *J. Mater. Chem. A*, 2017, **5**, 19431–19438.

37 Y. Zhao, H. Tan, H. Yuan, Z. Yang, J. Z. Fan, J. Kim, O. Voznyy, X. Gong, L. N. Quan, C. S. Tan, J. Hofkens, D. Yu, Q. Zhao and E. H. Sargent, *Nat. Commun.*, 2018, **9**, 1607.

38 W. Zia, C. A. Aranda, J. Pospisil, A. Kovalenko, M. Rai, C. Momblona, S. Gorji, G. Muñoz-Matutano and M. Saliba, *Chem. Mater.*, 2023, **35**, 5458–5467.

39 P. K. Nayak, D. T. Moore, B. Wenger, S. Nayak, A. A. Haghighirad, A. Fineberg, N. K. Noel, O. G. Reid, G. Rumbles, P. Kukura, K. A. Vincent and H. J. Snaith, *Nat. Commun.*, 2016, **7**, 13303.

40 Q. Lv, Z. Lian, Q. Li, J.-L. Sun and Q. Yan, *Chem. Commun.*, 2018, **54**, 1049–1052.

41 Y. Liu, Y. Zhang, X. Zhu, Z. Yang, W. Ke, J. Feng, X. Ren, K. Zhao, M. Liu, M. G. Kanatzidis and S. (Frank) Liu, *Sci. Adv.*, 2021, **7**, eabc8844.

42 Y. Liu, X. Zheng, Y. Fang, Y. Zhou, Z. Ni, X. Xiao, S. Chen and J. Huang, *Nat. Commun.*, 2021, **12**, 1686.

43 F. Wang, C. Ge, D. Duan, H. Lin, L. Li, P. Naumov and H. Hu, *Small Struct.*, 2022, **3**, 2200048.

44 Y. Wang, Y. Yang, N. Li, M. Hu, S. R. Raga, Y. Jiang, C. Wang, X.-L. Zhang, M. Lira-Cantu, F. Huang, Y.-B. Cheng and J. Lu, *Adv. Funct. Mater.*, 2022, **32**, 2204396.

45 S. Zhang, T. Xiao, F. Fadaei Tirani, R. Scopelliti, M. K. Nazeeruddin, D. Zhu, P. J. Dyson and Z. Fei, *Inorg. Chem.*, 2022, **61**, 5010–5016.

This journal is © The Royal Society of Chemistry 2024

J. Mater. Chem. C, 2024, **12**, 2953–2960 | **2959**

46 L. Chao, Y. Xia, X. Duan, Y. Wang, C. Ran, T. Niu, L. Gu, D. Li, J. Hu, X. Gao, J. Zhang and Y. Chen, *Joule*, 2022, **6**, 2203–2217.

47 A. Mahapatra, V. Anilkumar, R. D. Chavan, P. Yadav and D. Prochowicz, *ACS Photonics*, 2023, **10**, 1424–1433.

48 A. Mahapatra, N. Parikh, H. Kumari, M. K. Pandey, M. Kumar, D. Prochowicz, A. Kalam, M. M. Tavakoli and P. Yadav, *J. Appl. Phys.*, 2020, **127**, 185501.

49 Y. Liu, Y. Zhang, K. Zhao, Z. Yang, J. Feng, X. Zhang, K. Wang, L. Meng, H. Ye, M. Liu and S. (Frank) Liu, *Adv. Mater.*, 2018, **30**, 1707314.

50 Y. Cho, H. R. Jung, Y. S. Kim, Y. Kim, J. Park, S. Yoon, Y. Lee, M. Cheon, S. Jeong and W. Jo, *Nanoscale*, 2021, **13**, 8275–8282.

51 S. Zhang, T. Xiao, F. Fadaei Tirani, R. Scopelliti, M. K. Nazeeruddin, D. Zhu, P. J. Dyson and Z. Fei, *Inorg. Chem.*, 2022, **61**, 5010–5016.

52 S. Amari, J.-M. Verilhac, E. Gros D'Aillon, A. Ibanez and J. Zaccaro, *Cryst. Growth Des.*, 2020, **20**, 1665–1672.

53 T. W. Jones, A. Osherov, M. Alsari, M. Sponseller, B. C. Duck, Y.-K. Jung, C. Settens, F. Niroui, R. Brenes, C. V. Stan, Y. Li, M. Abdi-Jalebi, N. Tamura, J. E. Macdonald, M. Burghammer, R. H. Friend, V. Bulović, A. Walsh, G. J. Wilson, S. Lilliu and S. D. Stranks, *Energy Environ. Sci.*, 2019, **12**, 596–606.

54 A. Kalam, R. Runjhun, A. Mahapatra, M. M. Tavakoli, S. Trivedi, H. Tavakoli Dastjerdi, P. Kumar, J. Lewiński, M. Pandey, D. Prochowicz and P. Yadav, *J. Phys. Chem. C*, 2020, **124**, 3496–3502.

55 V. M. Le Corre, E. A. Duijnstee, O. El Tambouli, J. M. Ball, H. J. Snaith, J. Lim and L. J. A. Koster, *ACS Energy Lett.*, 2021, **6**, 1087–1094.

56 B. Murali, E. Yengel, C. Yang, W. Peng, E. Alarousu, O. M. Bakr and O. F. Mohammed, *ACS Energy Lett.*, 2017, **2**, 846–856.

57 K. M. Boopathi, B. Martín-García, A. Ray, J. M. Pina, S. Marras, M. I. Saidaminov, F. Bonaccorso, F. Di Stasio, E. H. Sargent, L. Manna and A. L. Abdelhady, *ACS Energy Lett.*, 2020, **5**, 642–649.

58 J. Oh, W. Y. Jeong, S. Y. Lee, B. Lee and M.-Y. Ryu, *Appl. Sci. Converg. Technol.*, 2020, **29**, 19–22.

59 H. Lu, H. Zhang, S. Yuan, J. Wang, Y. Zhan and L. Zheng, *Phys. Chem. Chem. Phys.*, 2017, **19**, 4516–4521.

60 S. Meloni, T. Moehl, W. Tress, M. Franckevičius, M. Saliba, Y. H. Lee, P. Gao, M. K. Nazeeruddin, S. M. Zakeeruddin, U. Rothlisberger and M. Graetzel, *Nat. Commun.*, 2016, **7**, 10334.

61 A. Mahapatra, V. Anilkumar, J. Nawrocki, S. V. Pandey, R. D. Chavan, P. Yadav and D. Prochowicz, *Adv. Elect. Mater.*, 2023, **9**, 2300226.

62 S. Gavranovic, J. Pospisil, O. Zmeskal, V. Novak, P. Vanysek, K. Castkova, J. Cihlar and M. Weiter, *ACS Appl. Mater. Interfaces*, 2022, **14**, 20159–20167.

2960 | *J. Mater. Chem. C*, 2024, **12**, 2953–2960

This journal is © The Royal Society of Chemistry 2024